molecules

MDPI

Article

Microstructure, Physical and Biological Properties, and BSA Binding Investigation of Electrospun Nanofibers Made of Poly(AA-co-ACMO) Copolymer and Polyurethane

Hanaa Mansour [1], Samia M. Elsigeny [1], Fawzia I. Elshami [1], Mohamed Auf [1], Shaban Y. Shaban [1,*] and Rudi van Eldik [2,3,*]

[1] Chemistry Department, Faculty of Science, Kafrelsheikh University, Kafrelsheikh 33516, Egypt; mansourhanaa@yahoo.com (H.M.); samia.elsigeny@sci.kfs.edu.eg (S.M.E.); fawzyaalshamy@yahoo.com (F.I.E.); mohamed.auf@sci.kfs.edu.eg (M.A.)
[2] Department of Chemistry and Pharmacy, University of Erlangen-Nuremberg, 91058 Erlangen, Germany
[3] Faculty of Chemistry, Nicolaus Copernicus University in Torun, 87-100 Torun, Poland
* Correspondence: shaban.shaban@sci.kfs.edu.eg (S.Y.S.); rudi.vaneldik@fau.de (R.v.E.)

Abstract: In this study, poly(AA-co-ACMO) and polyurethane-based nanofibers were prepared in a ratio of 1:1 (NF11) and 2:1 (NF21) as antimicrobial carriers for chronic wound management. Different techniques were used to characterize the nanofibers, and poly(AA-co-ACMO) was mostly found on the surface of PU. With an increase in poly(AA-co-ACMO) dose from 0 (PU) and 1:1 (NF11) to 2:1 (NF21) in the casting solution, the contact angle (CA) was reduced from 137 and 95 to 24, respectively, and hydrophilicity was significantly increased. As most medications inhibit biological processes by binding to a specific protein, in vitro protein binding was investigated mechanistically using a stopped-flow technique. Both NF11 and NF21 bind to BSA via two reversible steps: a fast second-order binding followed by a slow first-order one. The overall parameters for NF11 (K_a = 1.1 × 10^4 M^{-1}, K_d = 89.0 × 10^{-6}, ΔG^0 = −23.1 kJ mol^{-1}) and NF21 (K_a = 189.0 × 10^4 M^{-1}, K_d = 5.3 × 10^{-6} M, ΔG^0 = −27.5 kJ mol^{-1}) were determined and showed that the affinity for BSA is approximately (NF11)/(NF21) = 1/180. This indicates that NF21 has much higher BSA affinity than NF11, although BSA interacts with NF11 much faster. NF21 with higher hydrophilicity showed effective antibacterial properties compared to NF11, in agreement with kinetic data. The study provided an approach to manage chronic wounds and treating protein-containing wastewater.

Keywords: electrospun; poly(acrylic acid-co-acryloylmorpholine); nanofiber; hydrophilic; antibacterial; wound healing; BSA-affinity

check for updates

Citation: Mansour, H.; Elsigeny, S.M.; Elshami, F.I.; Auf, M.; Shaban, S.Y.; van Eldik, R. Microstructure, Physical and Biological Properties, and BSA Binding Investigation of Electrospun Nanofibers Made of Poly(AA-co-ACMO) Copolymer and Polyurethane. *Molecules* **2023**, *28*, 3951. https://doi.org/10.3390/molecules28093951

Academic Editors: Shaojun Yuan and Yuchao Zhao

Received: 17 April 2023
Revised: 5 May 2023
Accepted: 6 May 2023
Published: 8 May 2023

Copyright: © 2023 by the authors. Licensee MDPI, Basel, Switzerland. This article is an open access article distributed under the terms and conditions of the Creative Commons Attribution (CC BY) license (https://creativecommons.org/licenses/by/4.0/).

1. Introduction

Chronic skin wounds impose a significant medical burden on patients, particularly those with burns [1–4]. A good skin wound dressing must satisfy the following criteria [5]: good tissue compatibility, which avoids toxicity or inflammation [6,7], and good moisture retention, which keeps the wound moist and increases cell hydration [8], as well as suitable physical and mechanical durability, which ensures the dressing's integrity and prevents external bacterial infection caused by material damage [9].

For many years, N-acryloylmorpholine (ACMO) and its high molecular weight polymers have been researched [10]. ACMO is widely used in peptide synthesis, enzyme immobilization, blood plasma separation nanofibers, and drug release applications. Because ACMO has a disubstituted amide group, it can act as an acceptor in a hydrogen bond [11]. ACMO is a non-ionic, hydrophilic monomer and is also perfect for increasing the swelling ratio of hydrogels, allowing water to penetrate the polymeric network [12]. Poly(*N*-acryloylmorpholine) (PACMO) is a hydrophilic polymer with unique features

such as minimal toxicity and inhibition of in vivo immunological reactions [13,14]. Because of its high biocompatibility with the human body, PACMO has been employed in the transdermal delivery of active drugs [15]. Previous research has also shown that the PACMO-functionalized solid surface can reject non-specific protein adsorption [16–18]. PACMO's poor affinity for protein can be attributed to properties such as hydrophilicity, hydrogen bond acceptors, a lack of hydrogen bond donators, and electrical neutrality [19]. Electrospinning has evolved into a versatile technology for producing a wide range of fibers with diverse desired functions from a wide range of materials, including polymer–polymer blends [20–24], sol–gels [25,26], composites [27], and ceramics [28]. Owing to its good hydrophilicity and its polymer backbone with ionic pendant groups, acrylic acid (AA) was used by Sinah et al. to obtain a novel pH-responsive hydrophilic cross-linked poly(acrylic acid-co-acryloylmorpholine) (poly(AA-co-ACMO)) copolymer [29]. Because of its excellent chemical stability, adjustable mechanical performance, and outstanding biodegradability, polyurethane (PU) material has received much attention [30–33]. Grafting PU and poly(AA-co-ACMO) could be a way to combine the mechanical properties of PU with the hydrogel properties of poly(AA-co-ACMO). The addition of hydrophobic PU can also improve the longevity of poly(AA-co-ACMO) nanofibers in water [34].

Proteins are the most important biomolecules, and they are involved in a wide range of biological processes [35]. Protein–drug interactions, as well as protein structure serum albumin, which is found in blood plasma, are essential for drug transport and disposition in the biological system. Bovine serum albumin (BSA) has been extensively studied as a model protein for these interactions due to its structural similarity to human serum albumin [36]. Because its structure is similar to that of human serum albumin, the chosen BSA is an excellent model protein for studying interactions.

In this study, poly(AA-co-ACMO) in different ratios was blended with PU, and poly(AA-co-ACMO)/PU nanofibers (NF11 and NF21) were obtained using the electrospinning technique. A scanning electron microscope and FTIR spectroscopy were used to examine the surface morphology of the nanofibers and functionalization success, respectively. Furthermore, the thermal, contact angle measurements, and mechanical properties of the nanofibers were investigated. BSA-binding properties were studied to evaluate their pharmacological actions. Because protein–drug interaction is thought to be a fast step, we used a stopped-flow technique to analyze the binding process [37–40]. This technique aids in determining the kinetic characteristics of stages leading to intermediate species and, ultimately, obtaining an interaction mechanism. Additionally, the antibacterial activity is also reported and correlated with the kinetic parameters to evaluate the properties of electrospun nanofibers for chronic wound-dressing applications.

2. Results and Discussion

2.1. Characterization of Poly(AA-co-ACMO)/PU Nanofibers

Electrospun poly(AA-co-ACMO)/PU nanofibers were made in a 1:1 (*w*/*w*) (NF11) and 2:1 (*w*/*w*) (NF21) ratio, respectively, using electrospinning technology (See Figure 1).

The nanofibers PU, NF11, and NF21 were synthesized and characterized by FTIR in order to confirm the existence of functional groups in the copolymer, and Figure 2 shows the FTIR spectra of NF11 and NF21 nanofibers, as well as PU and poly(AA-co-ACMO)copolymers. The stretching vibrations of the -C-N bond present in PACMO are associated with the characteristic peak at 1509 cm^{-1} [41]. Furthermore, the peaks at 1256 cm^{-1} and 1098 cm^{-1} are caused by the stretching vibration of the C-O-C bond in the ACMO's morpholine ring. The stretching vibration of C=O of ACMO is responsible for another peak at 1660 cm^{-1} (NF11) and 1666 cm^{-1} (NF21). The spectra also show a peak around 1723 cm^{-1} that is attributed to the -COOH group in AA. The stretching vibration of the acrylic carboxylic –OH group was attributed to the peak at 3479 cm^{-1} observed in the region 3000–4000 cm^{-1}. Other peaks at 2932 and 2877 cm^{-1} are assigned for asymmetric stretching of the methylene groups (C-H of CH_2). A hydrogen-bonded carbonyl urethane group [42] was assigned to the presence of the peak at 1700 cm^{-1}. As a result, the FTIR spectra revealed that hydrogen bonding took place

in these nanofibers. Thus, the FTIR data of both synthesized NF11 and NF21 fibers contain all PACMO, AA, and PU characteristic peaks that are slightly shifted, indicating the presence of ACMO, AA, and PU in the nanofibers. Due to the increased feed ratio of poly(AA-co-ACMO), the intensity of all characteristic peaks of ACMO and AA was high in the NF21 nanofiber.

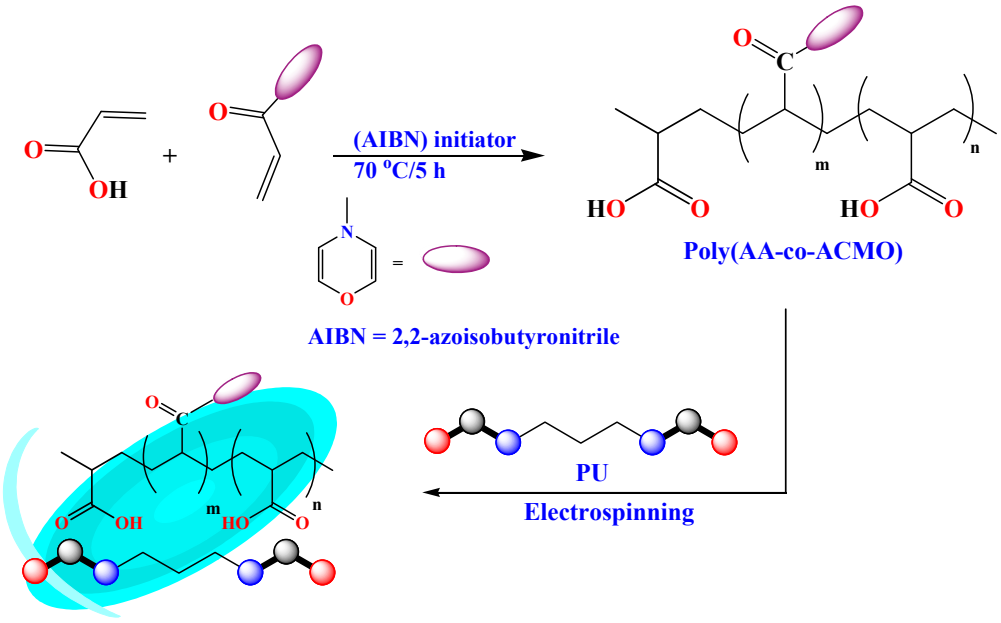

Figure 1. Synthetic reaction scheme of poly(AA-co-ACMO)/PU nanofibers during electrospinning.

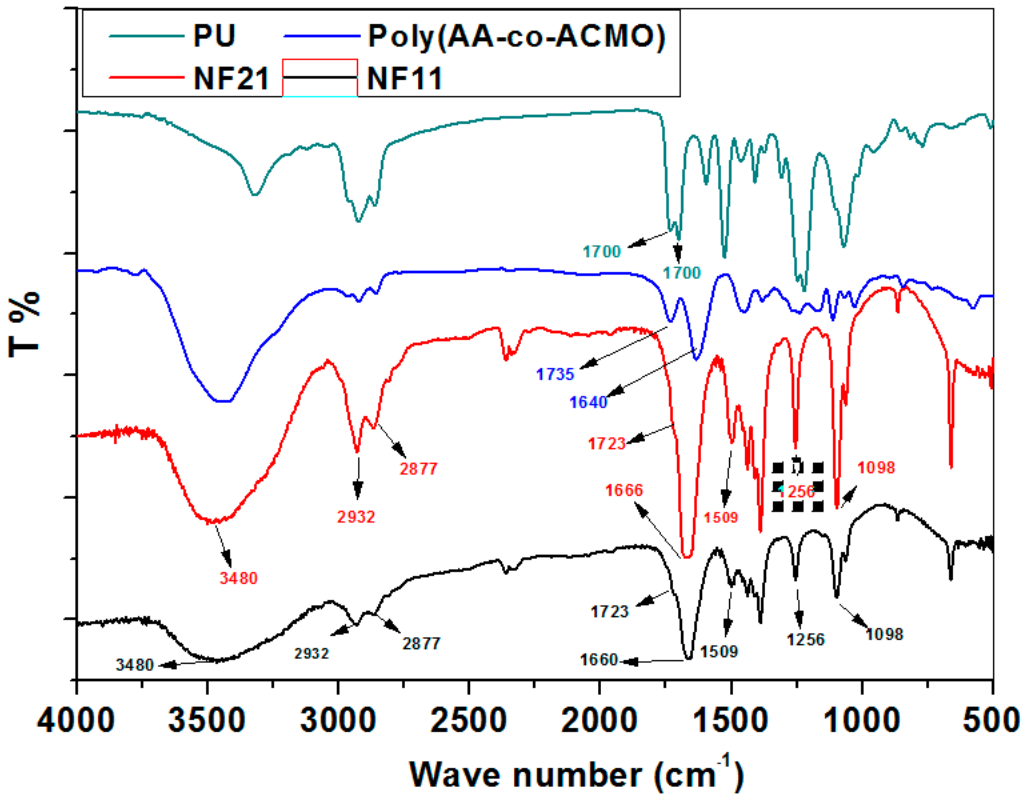

Figure 2. FTIR spectra of PU, poly(AA-co-ACMO), NF11, and NF21.

2.2. Hydrophilicity Analysis

Static water CA was used to determine the nanofibers' hydrophilicity. The hydrophilicity (lower hydrophobicity) of nanofibers increases as the CA value decreases and vice versa. Table 1 shows the static water contact angle of PU, NF11, and NF21 nanofibers measured with a goniometer, as well as the applied water droplets [25]. With an increase in poly(AA-co-ACMO) dose from 0, 1:1 to 2:1 in the casting solution, the CA is reduced from 137, 95 to 24° for PU, NF 11, and NF 21, respectively. The trend of the water CA of nanofibers was PU > NF11 > NF21, indicating that the CA decreased with the increase in poly(AA-co-ACMO) dose. These results show that the hydrophilicity of the NF21 nanofibers increased significantly by the addition of poly(AA-coACMO) content. The increased hydrophilicity of the nanofibers was entirely due to the poly(AA-co-ACMO)'s inherent hydrophilicity. The presence of the terminal carboxyl groups of the acrylic acid on the fibers considerably enhanced the hydrophilicity of the poly(AA-coACMO)/PU nanofibers' surface. Hydrophilicity increases the penetration of the liquid into the porosity to storage the water and as a consequence increases the uptake ability. By virtue of the CA results, the degree of hydrophilicity of the NF 21 nanofibers in the current study was relatively higher than the hydrophilicity found in previous studies [29,43].

Table 1. Water contact angles, tensile results, and average diameters of PU, NF11, and NF21 nanofibers.

Sample	PU	NF11	NF21
Water contact angle (°)	137.0 ± 4.0	95.0 ± 6.0	24.0 ± 1.5
Tensile strength (MPa)	5.2 ± 0.3	15.8 ± 1.0	8.5 ± 1.1
Young's modulus (MPa)	8.4 ± 0.6	46.0 ± 2.1	20.0 ± 2.3
Strain break (%)	3.4 ± 0.2	9.2 ± 1.2	6.7 ± 0.9

2.3. Morphology of Poly(AA-co-ACMO)/PU Blend Nanofibers

Electrospun nanofibers were used to assess the effect of poly(AA-co-ACMO on fiber morphology, and scanning electron microscopy (SEM) was used to investigate the difference in morphology between the electrospun nanofibers (Figure 3). Figure 3 displays SEM images of PU, NF11, and NF21 nanofibers, and more pictures with different magnifications are also presented in the supporting information (Supplementary Materials: Figures S1–S3). The structure and diameter of the electrospun nanofibers were greatly influenced by the variation in poly(AA-co-ACMO) concentrations. Micrographs of fibers electrospun at various poly(AA-co-ACMO) concentrations are shown in Figure 3.

The electrospinning process was observed to produce fibers in the absence of poly(AA-co-ACMO) (pure PU); however, as the concentration of poly(AA-co-ACMO) increased, electrospinning became more difficult due to the higher viscosity of the resulting solution, and the electrospun nanofiber displayed further non-smoothness and demonstrated a gluing between nanofibers (Figure 3b,c). The agglomeration of poly(AA-co-ACMO) and subsequent creation of the gluing nanofibers were brought on by the high viscosity and excess poly(AA-co-ACMO). The results suggested that the morphology of the electrospun nanofibers was influenced by the electrospinning solution's immiscibility. The SEM image of the PU is shown in Figure 3. As can be seen from this figure, the resulting fibers are quite uniform and smooth with a few structural defects. The increasing addition of poly(AA-co-ACMO) to PU leads to a decrease in the number of fine fibers, and some kinds of core–shell-like structures are formed, as shown in Figure 3a,b [44]. The findings suggested that PU, rather than poly(AA-co-ACMO), was the nanofiber's backbone [45].

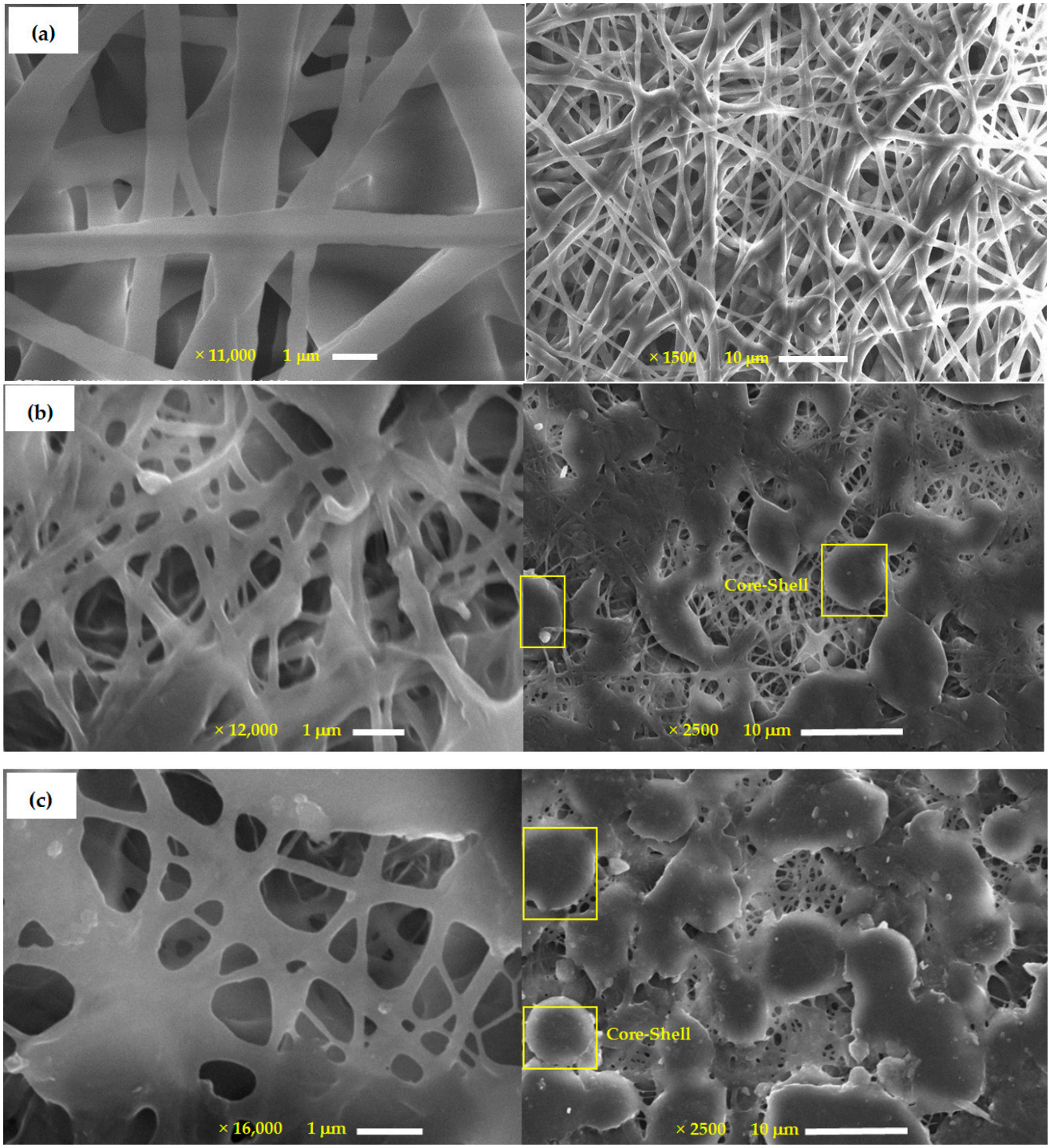

Figure 3. SEM images of the electrospun nanofibers: (**a**) PU; (**b**) NF11; and (**c**) NF21.

2.4. Mechanical Properties (Tensile Strength) Measurement

The mechanical properties of materials are known to be strongly influenced by microstructure and polymer interaction. The study of this property would yield valuable information about the internal structure of materials [46,47]. Figure 4 depicts the stress–strain behavior, Table 1 summarizes the mechanical properties, and more details are also presented in the supporting information (Table S1). Tensile measurements were taken in both the dry and wet states to assess the mechanical properties of the typical stress–strain curves of PU, NF11, and NF21 nanofibers.

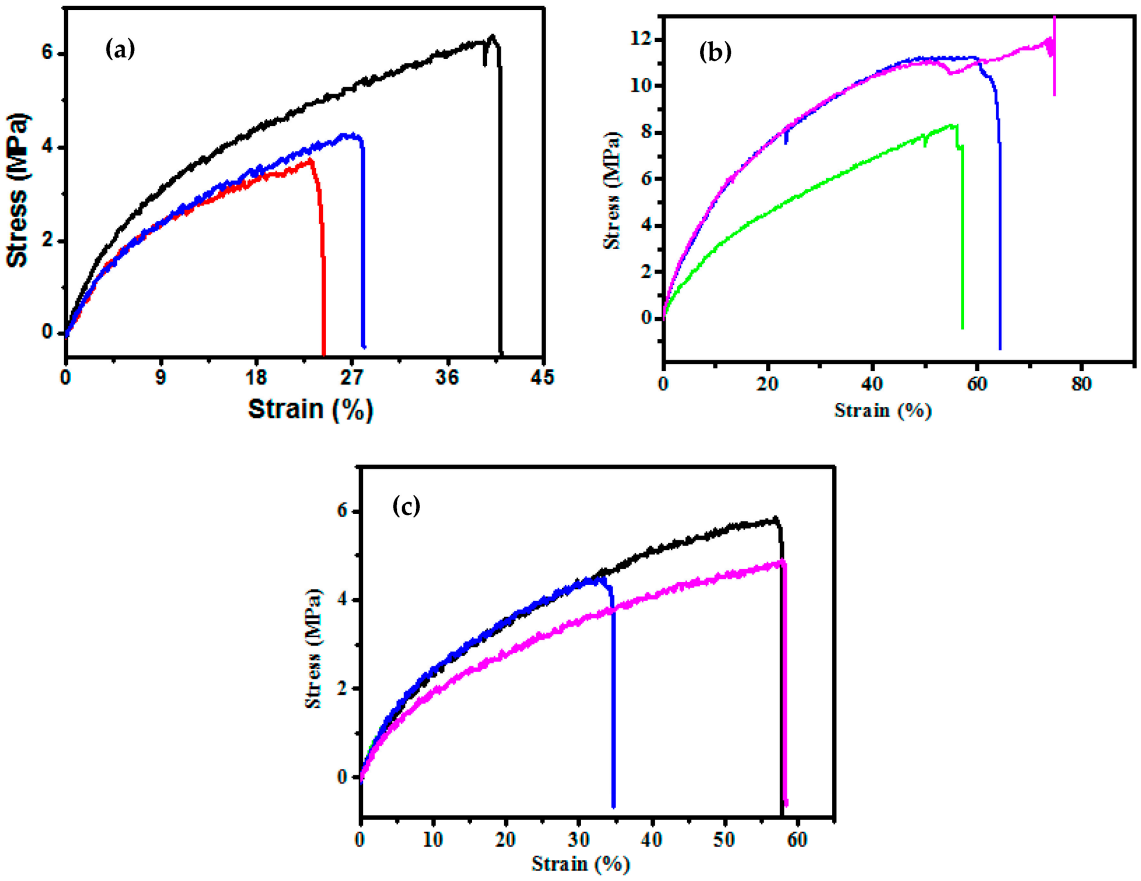

Figure 4. Tension stress–strain curves of (**a**) PU, (**b**) NF11, and (**c**) NF21.

The results reveal that improving the poly(AA-co-ACMO) content of the PU matrix enhances the mechanical properties. The best nanofiber is NF11 (loaded at a ratio of 1:1), which has a breaking point strain of 9.16% and an ultimate strength of 15.83 MPa. The nanofiber NF11 is therefore thought to have a stronger ability to resist compression deformation. It is important to note that adding more poly(AA-co-ACMO) does not raise or diminish the nanofibers' mechanical characteristics. Therefore, the poly(AA-co-ACMO) contents in the nanofiber should be adjusted in order to produce nanofibers with high mechanical performances.

It is understood that a significant interaction between the PU and poly(AA-co-ACMO) molecules is facilitated by the presence of many carboxyl groups on the poly(AA-co-ACMO) surface. Therefore, homogenous dispersion of the poly(AA-co-ACMO) in the PU matrix is preferred. When the amount of poly(AA-co-ACMO) is low, the interaction between the poly(AA-co-ACMO) molecules is weaker than the interaction between the poly(AA-co-ACMO) and the PU molecules, allowing the poly(AA-co-ACMO) to be dispersed uniformly throughout the PU matrix. The distance between poly(AA-co-ACMO) is shortened as the poly(AA-co-ACMO) loadings rise and the contact intensifies. Because of the aggregation, the poly(AA-co-ACMO) reinforcing function is lessened [48]. As a result, nanofibers' mechanical characteristics are enhanced. A strong interfacial adhesion and poly(AA-co-ACMO) dispersal and interaction with the polymer matrix are also essential for the poly(AA-co-ACMO) to make important contributions. On the other hand, the cross-linking of polymers may be prevented by the addition of a significant amount of poly(AA-co-ACMO). As a result, the cross-linking density decreases, increasing the quantity of equilibrium water that may sorb. Second, the polymerization of the monomers is hindered by the polymerization of the poly(AA-co-ACMO), which results in an inhomogeneous structure for the nanofibers.

According to the aforementioned description, low-poly(AA-co-ACMO) loadings (NF11) enhance the nanofibers' mechanical qualities, while high-poly(AA-co-ACMO) load-

ings cause them to decline (NF21). As a result, the concentration of poly(AA-co-ACMO) should be kept within reasonable limits [49,50].

2.5. Thermal Stability of the Composite Nanofibers

TGA was used to investigate PU, NF11, and NF21, as shown in Figure 5, which depicts the thermograms of nanofibers with two stages of thermal degradation. Until about 250 °C, all curves demonstrated stability and heat resistance. As the temperature rose further, the nanofibers began to degrade. The thermograms of NF11 and NF21 nanofibers were nearly identical, with a first stage at around 305 °C attributed to acrylic acid degradation. The ACMO moiety is degraded in the second stage, which occurs at 411 °C. PU11 had the highest T_g and the best TGA performance. A slightly higher mass retention for PU was observed across the entire temperature range, particularly between 250 and 600 °C, indicating better heat resistance in the lower temperature range. The first and second stages of PU were demonstrated at slightly higher temperatures (316, 416 °C) than both NF11 and NF21, indicating that PU has greater thermal stability. DTG thermograms (Figure 5) clearly showed that at around 300 °C, degradation of PU the copolymer was suppressed. As dw/dt was zero, the TG curves reached a plateau around 530 °C. Practically complete degradation is the fastest for PU and the char yield reached the lower value equal to 3%, whereas NF21 is the slowest and the char yield reached the higher value equal to 5%.

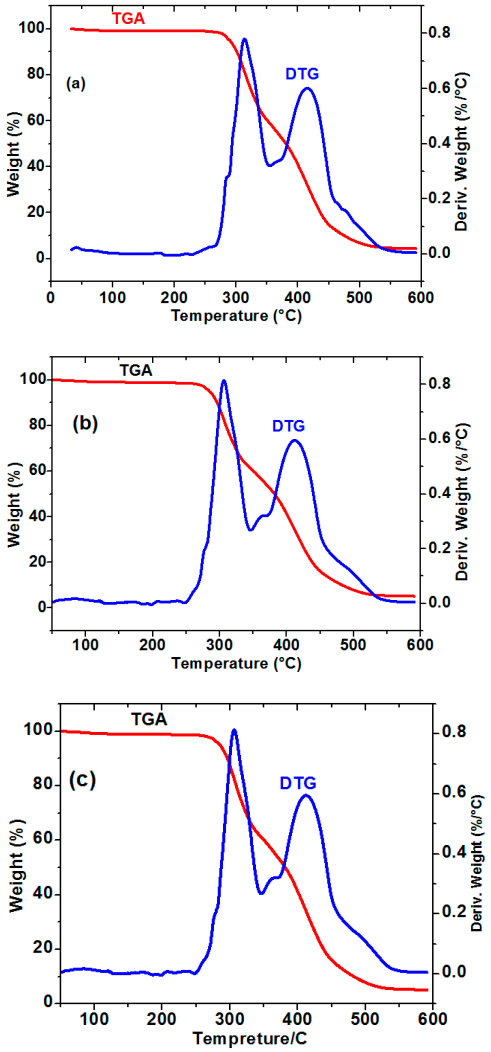

Figure 5. TGA and DTG curves of (**a**) PU, (**b**) NF11, and (**c**) NF21.

2.6. Antibacterial Activity Study

PU, NF11, and NF21 nanofibers were tested for antibacterial activity against *Staphylococcus aureus* and *Enterococcus faecalis* using the viable cell count method [51]. In this section, the minimal bactericidal concentration (MBC) is the lowest concentration of tested biocidal agents or fillers used to fill nanofiber mats that kill 99.9% of the initial bacterial colony. The relationship between the mean inhibition zone diameter and nanofiber concentrations is shown in Figure 6. The hydrophilic NF21 composite exhibited more effective antibacterial activity than the hydrophobic PU and NF11 composites, according to the antibacterial activity results. The formation of a core–shell-like fiber structure in the NF21 composite improved the hydrophilicity of PU. The nanofibers' adsorption onto the bacterial cell, diffusion through the cell wall, binding to the cytoplasmic membrane, release of cytoplasmic constituents such as K ions, DNA, and RNA, and cell wall damage disrupt the cell's natural processes and ultimately result in the rapid death of microorganisms in these dual actions.

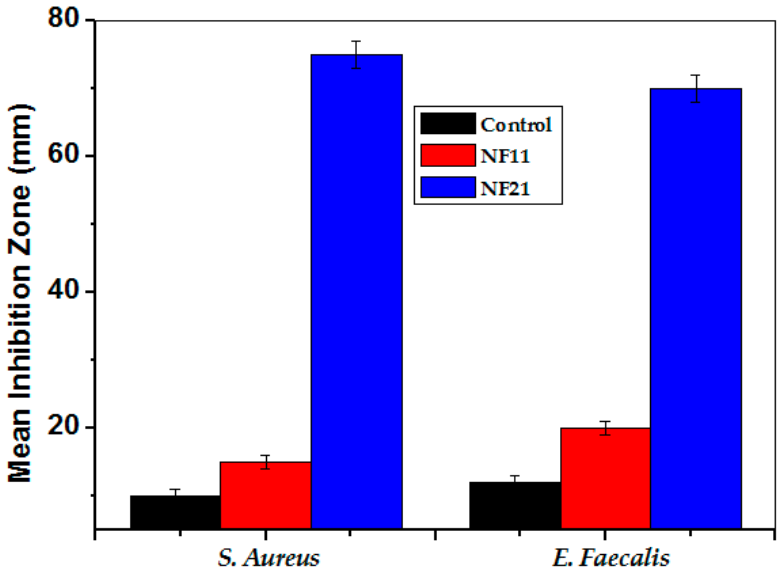

Figure 6. Antibacterial activity of PU, NF11, and NF21 against *S. aureus* and *E. faecalis* bacteria.

2.7. Mechanistic Investigation of BSA Binding

All of the studies have paid close attention to compounds that are linked to BSA, which appears to be a necessary but not the only factor influencing biological activity. Affinity, kinetics (rates) of association, and dissociation are all critical for biological activity [52]. These studies used the slowed-flow technique. The kinetic traces for the interaction with BSA can be observed at 270 nm. The kinetic curves cover the entire process and can be fitted to a two-exponential function, implying that at least two binding steps are involved, as shown by the UV–Vis spectra in Figure 7 as well as the kinetic traces shown in Figure 8. The first interaction step was found to be significantly faster than the second; 10^{-4} mol/L solutions of BSA were reacted with various concentrations of compounds while maintaining the pseudo-first-order reaction rate to see if the observed reaction rates were concentration-dependent. The plot of k_{obs} versus the concentration of NF11 and NF21 yielded a linear plot with a slope equal to k_1 and an intercept equal to k_{-1}, and the observed rate constant can be expressed by Equation (2) (Figure 9).

$$k_{obs} = k_1 + k_{-1}\,[\text{Nanofibers}] \quad (1)$$

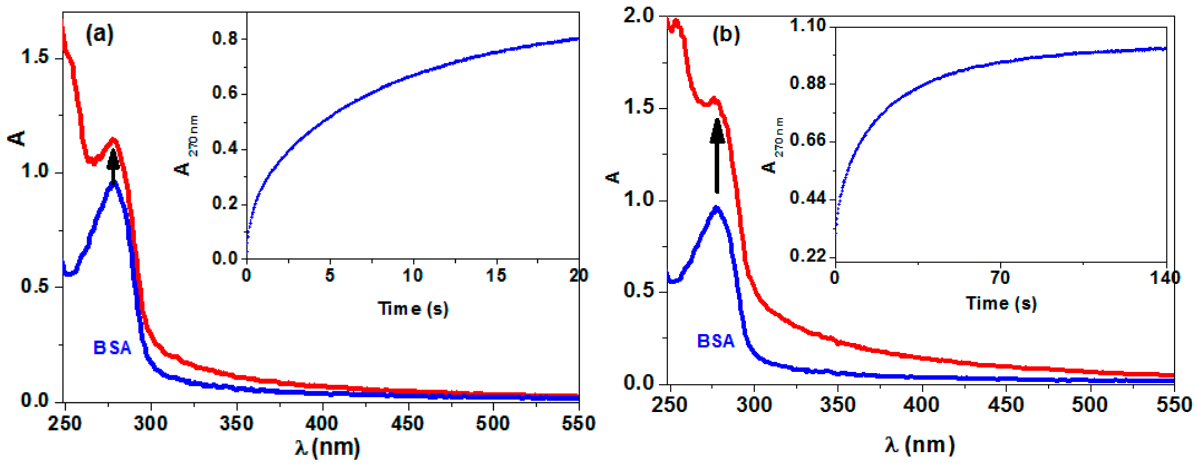

Figure 7. UV–vis spectra of BSA (1.0×10^{-4} M) before and after few seconds of the addition of (**a**) NF11 and (**b**) NF21 at 296 K.

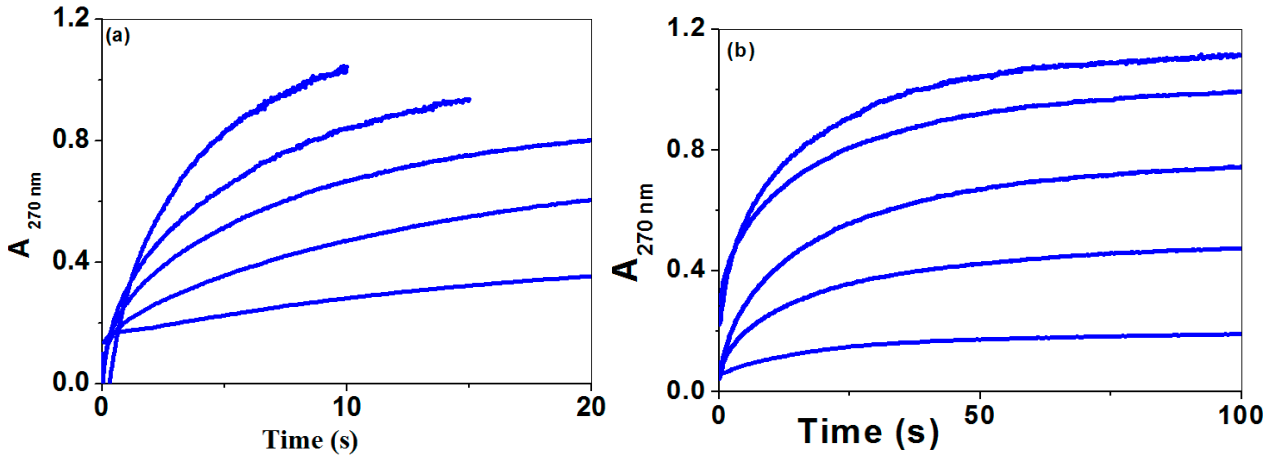

Figure 8. Kinetic traces of BSA interaction with (**a**) NF11 and (**b**) NF21 in methanol at 296 K.

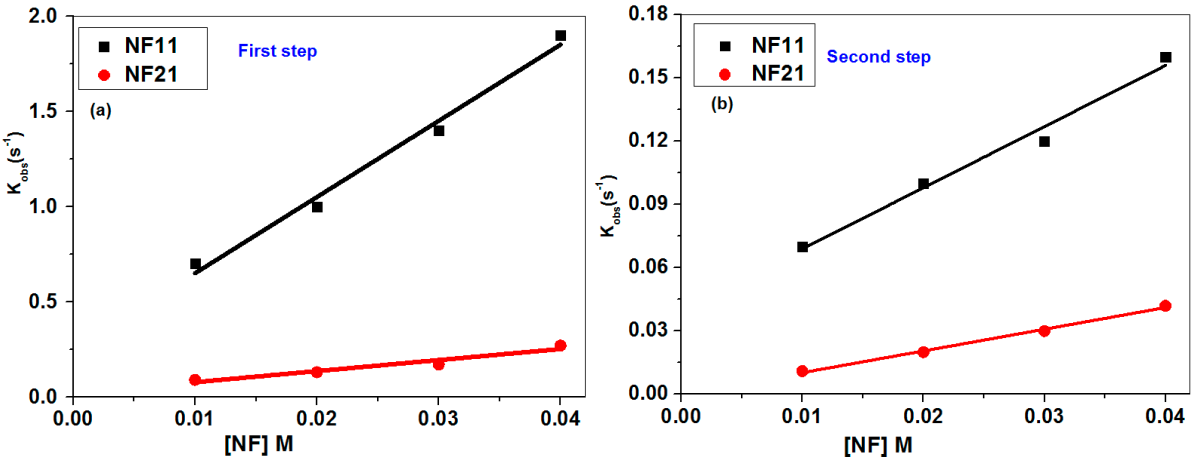

Figure 9. Plots of k_{obs} vs. nanofiber concentrations during the (**a**) first and (**b**) second steps of the BSA interaction.

Here, k_1 and k_{-1} are rate constants that describe the first step kinetics of BSA complex formation as well as dissociation. The first steps in Scheme 1 express this fast and reversible step of BSA binding, which includes compound formation and dissociation.

$$\textbf{NF11/NF21 + BSA} \underset{k_{-1}}{\overset{k_1}{\rightleftharpoons}} \textbf{NF11/NF21–BSA complex} \underset{k_{-2}}{\overset{k_2}{\rightleftharpoons}} \textbf{Adduct product}$$

Scheme 1. BSA binding reaction scheme for NF11 and NF21.

BSA binds reversibly to NF11 with a second-order association constant of $k_1 = 45.7 \pm 4.5\ M^{-1}s^{-1}$ in the initial phase and dissociates from the binary complex with a first-order dissociation constant of $k_{-1} = 0.257 \pm 0.013\ s^{-1}$. In contrast, NF21 binds to BSA eight times slower ($k_1 = 6.2 \pm 0.4\ M^{-1}s^{-1}$) and dissociates about thirty times slower ($k_{-1} = 7.3 \pm 1.3\ s^{-1}$). This means that BSA's binding affinity for NF11, K_{a1}, $k_1/k_{-1} = 178\ M^{-1}$ is about five times lower than that of NF21 ($827\ M^{-1}$) and that BPA's equilibrium dissociation constant, K_{d1}, $k_{-1}/k_1 = 6 \times 10^{-3}$ M, is about five times higher than that of NF21 (1×10^{-3} M). This means that the NF21–BSA that has been formed is far more stable than NF11–BSA. The equilibrium dissociation constant, K_{d1}, is related to the difference between the free energy, G, of BSA molecules alone in the solution and when bound together. The binding free energy change G_{bind} is calculated using Equation (3).

$$\Delta G_{bind} = RT \cdot ln(K_d) \quad (2)$$

While T and R represent the absolute temperature and the universal gas coefficient, respectively, the ΔG_{bind} values, calculated using Equation (4), are -12.6 and -17.1 kJ mol^{-1} for the first step binding of BSA to NF11 and NF21, respectively. The negative sign for G indicates spontaneous binding to both NF11 and NF21, and the greater negative value of NF21 compared to NF11 indicates that binding with NF21 is very favorable. The data from the second reaction step, primarily concerned with the BSA condensation process, in addition to the electrostatic interaction, followed the same pattern as the first; a reversible reaction was observed for both NF11 and NF21. The BSA affinity for NF11 ($K_{a2} = k_2/k_{-2}$) is 65.9 M^{-1}, which is about thirty times lower than NF21 ($1900\ M^{-1}$), and the equilibrium dissociation constant for NF11 ($K_{d2} = k_{-2}/k_2$) is 15.0×10^{-3} M, which is about thirty times faster than NF21 (0.53×10^{-3} M). G_{bind} values for this phase are -6.7 kJ mol^{-1} (NF11) and -18.7 kJ mol^{-1} (NF21), indicating that binding with NF21 is very favorable as the first step. Equation (4) shows how to calculate the overall equilibrium dissociation constant, K_d, from the individual equilibrium dissociation constants, K_{d1} and K_{d2}, as well as the overall association constants, K_a.

$$K_d = \frac{K_{d1}K_{d2}}{1 + K_{d2}} \quad (3)$$

The data in Table 2 show that the overall BSA binding affinity of NF21 (189×10^4 M) is much higher than that of NF11 (1.1×10^4 M). The overall reaction G_{bind} values are -23.1 kJ mol^{-1} (NF11) and -27.5 (NF21) kJ mol^{-1}, indicating that the reaction is spontaneous for both compounds. This means that when the dose of copolymer poly(AA-co-ACMO) in the casting solution was increased, the value of BSA binding affinity increased. These findings show that blending poly(AA-co-ACMO) copolymers enhanced the BSA affinity at the nanofibers' interface. Increases in hydrophilicity of poly(AA-co-ACMO)/PU (decrease in CA) were the cause, as previously stated. The poly(AA-co-ACMO) content was higher in NF21 nanofibers and lower in NF11 nanofibers, resulting in a BSA affinity trend of NF11 > NF21. The following factors could explain this phenomenon: van der Waals interactions between water and the membrane surface; electrostatic repulsion between the membrane surface and protein [50] due to the hydrophilic layer; and hydration interactions as a result of water layer formation linked to the hydrophilic additive that produces a repulsive force towards protein [29,43].

Table 2. Rate constants, affinities, and dissociation constants recorded during the reaction of BSA with NF11 and NF21.

	Activation Parameters	NF11	NF21
First interaction step	k_1 [M^{-1} s^{-1}]	45.7 ± 4.5	6.2 ± 0.4
	k_{-1} [10^{-3} s^{-1}]	257.0 ± 13.6	7.5 ± 1.3
	K_{a1} [M^{-1}]	177.8	826.6
	K_{d1} [10^{-3} M]	6.0	1.0
	$\Delta G_1^{\#}$ [kJ mol^{-1}]	−12.6	−17.1
Second interaction step	K_2 [M^{-1} s^{-1}]	2.9 ± 0.2	1.9 ± 0.1
	k_{-2} [10^{-3} s^{-1}]	44.0 ± 1.0	1.0 ± 0.1
	K_{a2} [M^{-1}]	66	1900
	K_{d2} [10^{-3} M]	15.0	0.5
	$\Delta G_2^{\#}$ [kJ mol^{-1}]	−6.7	−18.7
Overall interaction data	K_d [10^{-6} M]	89	5.3
	K_a [10^4 M]	1.1	189
	$\Delta G^{\#}$ [kJ mol^{-1}]	−23.1	−27.5

3. Materials and Methods

3.1. Materials

The following items were purchased: ACMO (Aldrich, Milwaukee, WI, USA), AA (Merck, Stuttgart, Germany), 2,2-azoisobutyronitrile (AIBN) as an initiator, and PU (Noveon BVBA, Chaussee de Wavre 1945, B- 1160 1160 Brussels). The rest of the reagents were used without purification. A BSA stock solution (1×10^{-3} mol/L) was prepared in Tris buffer at pH 7.4 using bovine serum albumin (BSA, Sigma-Aldrich, Burlington, MA, USA). Solutions (4×10^{-4} mol/L) were prepared in Tris buffer from the first stock solution to a lower concentration of ethanol during sequential addition in titrations with BSA (to avoid ethanol's effect on BSA structure, concentrations of ethanol were kept below 1% (wt/wt) for all titrations [53]).

3.2. Synthesis Poly(AA-co-ACMO) Copolymer

Poly(AA-co-ACMO) was synthesized as previously reported [54]. In a nutshell, acryloyl morpholine (ACMO) (5 mL, 0.04 mol), acrylic acid (AA) (3 mL, 0.04 mol), and azoisobutyronitrile (AIBN) (0.0651 g, 0.00039 mol) were dissolved in 10 mL of dry toluene. The polymerization mixture was kept at 70 °C for 5 h under N_2 atmosphere. The polymer was then filtered, washed with methanol, and dried at 40 °C until a consistent weight was achieved. The success rate was 95%.

3.3. Fabrication of poly(AA-co-ACMO)/PU (NF11 and NF21)

To form uniform solutions, poly(AA-co-ACMO) and PU were dissolved in a mixture of chloroform/dichloromethane solution (7 mL:3 mL) by stirring for 8 h at room temperature. Poly(AA-co-ACMO) to PU component ratios were 1:1 (*w*/*w*) and 2:1 (*w*/*w*). The solution was dispensed into a 10 mL syringe fitted with a 0.25 mm inner diameter metal needle. The solution flow rate was set to 4 mL h^{-1} with a 60 kV applied voltage. The tip-to-collector distance was 16 cm, and the collector was a grounded aluminum sheet. The electrospun nanofiber film was dried in an air oven at 50 °C for 24 h to thoroughly eliminate the residual solvent.

3.4. Morphology and Characterization of Nanofibers

A field emission electron microscope (SEM) was used to examine the surfaces of the electrospun nanofibers (TESCAN Vega 3, 5 kV, 5 mm working distance, SE detector). The nanofibers were identified using FTIR spectra recorded at room temperature with a spectrometer (Perkin–Elmer, Waltham, MA) and measured in the wavenumber range 4000 to 400 cm^{-1} by dispersing them in KBr matrices. The thermal behavior of the nanofiber was studied using

thermogravimetric analysis (TGA, STA449F3; NETZSCH, Selb, Germany). Under a nitrogen atmosphere, the heating rate is 10 °C/min, with a heating range of 25 to 800 °C.

3.5. Contact Angle Measurement

Under ambient conditions, the dynamic contact angles of nanofibers were measured under ambient conditions using a contact angle meter (DSA 25; KRUSS, Hamburg, Germany). Deionized water was chosen as the liquid for contact angle measurement. A water droplet (0.05 mL) was placed on the nanofiber membrane's surface, and the contact angle was measured for 1 to 30 s.

3.6. Mechanical Measurement

Mechanical tensile tests were performed with a TA Instruments Discovery Hybrid Rheometer D-HR3 equipped with linear tensile geometries dedicated to film characterization. Large scaffolds were cut into rectangular samples with a 5 mm width, 22 mm length, and a thickness of less than 100 microns and clamped. Each sample's thickness was meticulously measured using a scanning electron microscope (SEM) examination of each cross section. The sample length between the clamps was initially set to 10 mm, the tensile velocity was set to 50 m/s, and the temperature was set to 21 °C. The samples were first fixed in the clamps at dry state and then hydrated in distilled water before starting the tensile test to characterize the scaffolds in the wet state.

3.7. Antibacterial Ability Test

The viable cell count method [55] was used to assess the antimicrobial ability of PU, NF11, and NF21 nanofibers. The antibacterial activity of the prepared nanofibers was tested using two bacterial strains (*E. faecalis* and *E. coli*). Bacterial strains were inoculated in LB broth medium containing Tryptone (1%), yeast extract (0.5%), and NaCl (1%) at pH 7 and incubated overnight at 37 °C in a shaking incubator (Model InnovaTMJ-25, New Brunswick Scientific, Edison, NJ, USA) for refreshment. With LB broth medium (1%), the bacteria suspensions were diluted up to 100 times. A volume of 100 L of diluted suspension was cultured in 10 mL of Tryptone medium containing 0.1 g of tested sample and then sterilized for at least 20 min at 121 °C. The mixture was then left to sit for a while. After that, the mixture was shaken for 18 h at 37 °C, and the percentage of bacteria growth inhibition was determined by measuring the absorbance of the culture medium at 600 nm using visible spectroscopy. The inhibition (percentage) was calculated using the equation below:

$$\text{Inhibition (\%)} = (A_a - A_b)/A_a \times 100 \quad (4)$$

where A_b and A_a are the absorbance of bacterial culture in absence and in presence of tested sample, respectively.

3.8. BSA Binding Studies

In methanol, stock solutions of nanofibers (10^{-3} mol/L) were prepared, which were then diluted to make working solutions for spectroscopic methods. Phosphate-buffered solution (PBS) at pH 7.4 was used to make all of the solutions. All of the experiments were carried out at a pH of 7.4 and at room temperature. At 240–360 nm, the absorption spectra of BSA were recorded in the absence and presence of increasing amounts of nanofibers. The spectral changes in the reactions were first recorded over the wavelength range of 200–700 nm for stopped-flow measurements, and the kinetic traces were recorded at 270 nm. Using at least a 10-fold number of nanofibers, all reactions were studied under pseudo-first-order conditions. By fitting absorbance time traces to a two-exponential function, the pseudo-first-order rate constant was investigated. Under each set of experimental conditions, all listed rate constants are the average of at least two independent kinetic runs.

4. Conclusions

Poly(AA-co-ACMO) and PU-based electrospun nanofibers are being developed for use as antimicrobial carriers in chronic wound treatment. To improve the hydrophilicity of electrospun PU nanofibers, various amounts of poly(AA-co-ACMO) were added to PU, and poly(AA-co-ACMO) was mostly found on the PU nanofibers' surfaces. Increasing the dose of poly(AA-co-ACMO) in the casting solution reduces contact angles, thereby enhancing the hydrophilicity of the surface of poly(AA-co-ACMO)/PU nanofibers. Because almost all pharmaceuticals work by interfering with biological functions by binding to a specific protein, in vitro protein binding of both nanofibers was studied mechanistically using a stopped-flow technique and a mechanism was proposed. NF11 and NF21 bind to BSA in a similar way, with two reversible steps: a fast second-order binding followed by a slow first-order one. The overall binding parameters were determined and showed that the relative affinity for BSA is approximately (NF11)/(NF21) = 1/180. This suggests that, despite the fact that BSA interacts with NF11 significantly faster, NF21 has a much higher affinity for BSA. This is because the rapid association of NF11 with BSA is followed by a fast dissociation reaction. Higher *K*a values (10^5 to 10^7 M^{-1}) compared to that reported in the literature are associated with high degrees of binding (90% to 99.9%) [56,57]. The increased hydrophilicity nanofibers NF21 demonstrated good antibacterial capabilities compared to the less hydrophilic NF11, which is consistent with the protein-binding affinity. These results can be used to estimate the impact of protein binding on antimicrobial killing for various antibiotics and bacteria [58], and this research could lead to a new method of managing chronic wounds and treating protein-containing wastewater.

Supplementary Materials: The following supporting information can be downloaded at: https://www.mdpi.com/article/10.3390/molecules28093951/s1, Figure S1. SEM images of the electrospun nanofibers PU: Figure S2. SEM images of the electrospun nanofibers NF11: Figure S3. SEM images of the electrospun nanofibers NF21; Table S1. Tensile results of PU, NF11 and NF21 nanofibers.

Author Contributions: H.M.: Methodology, supervision, draft writing, revision; S.M.E.: project administration, revision; supervision; F.I.E.: investigation, data curation; M.A.: investigation, methodology, draft writing; S.Y.S.: project administration, writing and revision; R.v.E.: project administration, revision. All authors have read and agreed to the published version of the manuscript.

Funding: This research received no external funding.

Institutional Review Board Statement: Not applicable.

Informed Consent Statement: Not applicable.

Data Availability Statement: Not applicable.

Conflicts of Interest: The authors declare that there are no conflict of interest regarding the publication of this research paper.

References

1. Shah, S.A.; Sohail, M.; Khan, S.; Minhas, M.U.; De Matas, M.; Sikstone, V.; Hussain, Z.; Abbasi, M.; Kousar, M. Biopolymer-based biomaterials for accelerated diabetic wound healing: A critical review. *Int. J. Biol. Macromol.* **2019**, *139*, 975–993. [CrossRef]
2. Silva, L.P.D.; Reis, R.L.; Correlo, V.M.; Marques, A.P. Hydrogel-Based Strategies to Advance Therapies for Chronic Skin Wounds. *Annu. Rev. Biomed. Eng.* **2019**, *21*, 145–169. [CrossRef] [PubMed]
3. Ramos-Gallardo, G. Chronic Wounds in Burn Injury: A Case Report on Importance of Biofilms. *World J. Plast. Surg.* **2016**, *5*, 175–180.
4. Frykberg, R.G.; Banks, J. Challenges in the Treatment of Chronic Wounds. *Adv. Wound Care* **2015**, *4*, 560–582.
5. Liang, Y.; He, J.; Guo, B. Functional Hydrogels as Wound Dressing to Enhance Wound Healing. *ACS Nano* **2021**, *15*, 12687–12722. [CrossRef]
6. Xi, Y.; Ge, J.; Wang, M.; Chen, M.; Niu, W.; Cheng, W.; Xue, Y.; Lin, C.; Lei, B. Bioactive Anti-inflammatory, Antibacterial, Antioxidative Silicon-Based Nanofibrous Dressing Enables Cutaneous Tumor Photothermo-Chemo-Therapy and Infection Induced Wound Healing. *ACS Nano* **2020**, *14*, 2904–2916. [CrossRef] [PubMed]

7. Wang, M.; Niu, W.; Chen, M.; Cheng, W.; Zhang, L.; Xie, C.; Wang, Y.; Guo, Y.; Leng, T.; Zhang, X.; et al. Injectable self-healing anti-inflammatory europium oxide-based dressing with high angiogenesis for improving wound healing and skin regeneration. *Chem. Eng. J.* **2021**, *412*, 128471–128479.
8. Ousey, K.; Cutting, K.F.; Rogers, A.A.; Rippon, M.G. The importance of hydration in wound healing: Reinvigorating the clinical perspective. *J. Wound Care* **2016**, *25*, 122–130. [CrossRef]
9. Lustig, A.; Gefen, A. Three-dimensional shape-conformation performances of wound dressings tested in a robotic sacral pressure ulcer phantom. *Int. Wound J.* **2021**, *18*, 670–680. [CrossRef]
10. Ashkezari, M.M.; Shokrollahi, P.; Zandi, Z.; Shokrolahi, F. Polyurethanes with separately tunable biodegradation behaviorand mechanical properties for tissue engineering. *Polym. Adv. Technol.* **2018**, *2*, 528–541.
11. Efe, H.; Bicen, M.; Kahraman, M.V.; Kayaman-Apohan, N. Synthesis of 4-Acryloylmorpholine-based Hydrogels and Investigation of their Drug Release Behaviors. *J. Braz. Chem. Soc.* **2013**, *24*, 814–820. [CrossRef]
12. Schiavon, O.; Caliceti, P.; Ferruti, P.; Veronese, F.M. Therapeutic proteins: A comparison of chemical and biological properties of uricase conjugated to linear or branched poly(ethylene glycol) and poly(N-acryloylmorpholine). *Il Farmaco* **2000**, *55*, 264–269. [CrossRef] [PubMed]
13. Jo, Y.K.; Vlies, A.J.V.; Gantz, J.; Antonijevic, S.; Demurtas, D.; Velluto, D.; Hubbell, J.A. RAFT homo- and copolymerization of *N*-acryloyl-morpholine, piperidine, and azocane and their self-assembled structures. *Macromolecules* **2008**, *41*, 1140–1150. [CrossRef]
14. Torchilin, V.P.; Shtilman, M.I.; Trubetskoy, V.S.; Whiteman, K.; Milstein, A.M. Amphiphilic vinyl polymers effectively prolong liposome circulation time in vivo. *Biochim. Biophys. Acta* **1994**, *1195*, 181–184. [CrossRef] [PubMed]
15. Fares, M.M.; Al-Shboul, A.M. Stimuli pH-responsive (N-vinylimidazole-co-acryloylmorpholine) hydrogels; mesoporous and nanoporous scaffolds. *J. Biomed. Mater. Res. Part A* **2010**, *100*, 863–871.
16. Takahashi, H.; Nakayama, M.; Shimizu, S.; Yamato, M.; Okano, T. Anisotropic cell sheets for constructing three-dimensional tissue with well-organized cell orientation. *Biomaterials* **2011**, *32*, 8830–8838. [CrossRef]
17. Takahashi, H.; Nakayama, M.; Itoga, K.; Yamato, M.; Okano, T. Micropatterned thermoresponsive polymer brush surfaces for fabricating cell sheets with well-controlled orientational structures. *Biomacromolecules* **2011**, *12*, 1414–1418. [CrossRef]
18. Kruk, T.; Bzowska, M.; Hinz, A.; Szuwarzyński, M.; Szczepanowicz, K. Control of Specific/Nonspecific Protein Adsorption: Functionalization of Polyelectrolyte Multilayer Films as a Potential Coating for Biosensors. *Materials* **2021**, *14*, 7629. [CrossRef]
19. Greiner, A.; Wendorff, H. Electrospinning: A fascinating method for the preparation of ultrathin fibers. *Angew. Chem. Int. Ed.* **2007**, *46*, 5670–5673. [CrossRef]
20. Lin, S.; Cai, Q.; Ji, J.; Sui, G.; Yu, Y.; Yang, X. Electrospun nanofiber reinforced and toughened composites through in situ nano-interface formation. *J. Compos. Sci. Technol.* **2008**, *68*, 3322–3329. [CrossRef]
21. Park, S.J.; Chase, G.G.; Jeong, K.; Kim, H.Y. Mechanical properties of titania nanofiber mats fabricated by electrospinning of sol–gel precursor. *J. Sol.-Gel. Sci. Technol.* **2010**, *54*, 188–194. [CrossRef]
22. Sekak, A.; Lowe, A. Structural and Thermal Characterization of Calcium Cobaltite Electrospun Nanostructured Fibers. *J. Am. Ceram. Soc.* **2011**, *94*, 611–619. [CrossRef]
23. Yu, H.; Xu, Y.; Havener, K.; Zhang, M.; Zhang, L.; Wu, W.; Huang, K. Temperature-Controlled Selectivity of Hydrogenation and Hydrodeoxygenation of Biomass by Superhydrophilic Nitrogen/Oxygen Co-Doped Porous Carbon Nanosphere Supported Pd Nanoparticles. *Small* **2022**, *18*, 2106893–2106903. [CrossRef] [PubMed]
24. Yu, H.; Zhang, L.; Gao, S.; Wanga, H.; He, Z.; Xu, Y.; Huang, K. In situ encapsulated ultrafine Pd nanoparticles in nitrogen-doped porous carbon derived from hyper-crosslinked polymers effectively catalyse hydrogenation. *J. Catal.* **2021**, *396*, 342–350.
25. Zhu, J.; Wei, S.; Rutman, D.; Haldolaarachchige, N.; Young, D.; Guo, Z. Magnetic polyacrylonitrile-Fe@FeO nanocomposite fibers—Electrospinning, stabilization and carbonization. *J. Polym.* **2011**, *52*, 2947–2955. [CrossRef]
26. Zhu, J.; Wei, S.; Patil, R.; Rutman, D.; Kucknoor, S.; Wang, A.; Guo, Z. Ionic liquid assisted electrospinning of quantum dots/elastomer composite nanofibers. *J. Polym.* **2011**, *52*, 1954–1962. [CrossRef]
27. Chen, X.; Wei, S.; Gunesoglu, C.; Zhu, J.; Southworth, S.; Sun, L. Electrospin Magnetic Fibrillar Polystyrene Nanocomposites Reinforced with Nickel Nanoparticles. *J. Macromol. Chem. Phys.* **2010**, *211*, 1775–1783. [CrossRef]
28. Zhang, D.; Karki, A.; Rutman, D.; Young, D.; Wang, A.; Cocke, D.; Ho, T.; Guo, Z. Electrospin polyacrylonitrile nanocomposite fibers reinforced with Fe3O4 nanoparticles: Fabrication and property analysis. *J. Polym.* **2009**, *50*, 4189–4198. [CrossRef]
29. Sainia, B.; Khuntiab, S.; Sinha, M.K. Incorporation of cross-linked poly(AA-co-ACMO) copolymer with pH responsive and hydrophilic properties to polysulfone ultrafiltration membrane for the mitigation of fouling behavior. *J. Membr. Sci.* **2019**, *572*, 184–197. [CrossRef]
30. El-Refaie, K.; Gary, L.; Kevin, M.; John, L.; David, S.; Elliot, H.; Gary, W. Release of tetracycline hydrochloride from electrospun poly(ethylene-co-vinylacetate), poly(lactic acid), and a blend. *J. Control Rel.* **2002**, *81*, 57–64.
31. Arefin, J.H.A.; Huang, D.; Platts, V.D.; Hypes, J.F.; Harris, R.; Iyer, P.N. Fabrication of flexible thin polyurethane membrane for tissue engineering applications. *Biomed. Microdevices* **2017**, *19*, 98–106. [CrossRef]
32. Li, Y.H.; Li, N.; Pan, W.; Yu, Z.Z.; Yang, L.M.; Tang, B. Hollow mesoporous silica nanoparticles with tunable structures for controlled drug delivery. *ACS Appl. Mater. Interfaces* **2017**, *9*, 2123–2129. [CrossRef] [PubMed]
33. Yi, J.Z.; Goh, S.H. Interactions in miscible blends and complexes of poly(N-acryloylmorpholine) with poly(p-vinylphenol). *Polymer* **2002**, *43*, 4515–4522. [CrossRef]

34. Li, D.; Lin, J.; An, Z.; Li, Y.; Zhu, X.; Yang, J.; Wang, Q.; Zhao, J.; Zhao, Y.; Chen, L. Enhancing hydrophilicity and comprehensive antifouling properties of microfiltration membrane by novel hyperbranched poly(N-acryoylmorpholine) coating for oil-in-water emulsion separation. *React. Funct. Polym.* **2020**, *156*, 104735. [CrossRef]
35. Suryawanshi, V.D.; Anbhule, P.V.; Gore, A.H. Spectroscopic investigationon the interaction of pyrimidine derivative, 2-amino-6-hydroxy-4-(3,4-di-methoxyphenyl)-pyrimidine-5-carbonitrile with human serum albumin: Mechanistic and conformational study. *Ind. Eng. Chem. Res.* **2012**, *51*, 95–102. [CrossRef]
36. Peters, T. *All about Albumin: Biochemistry, Genetics and Medical Application*; Academic Press: New York, NY, USA, 1996.
37. Shaban, N.Z.; Yehia, S.A.; Shoueir, K.R.; Saleh, S.R.; Awad, D.; Shaban, S.Y. Design, DNA binding, and kinetic studies, antibacterial and cytotoxic activities of stable dithiophenolato titanium(IV)-chitosan Nanocomposite. *J. Mol. Liq.* **2019**, *287*, 111002. [CrossRef]
38. Shaban, N.Z.; Aboelsaad, A.M.; Shoueir, K.R.; Abdulmalek, S.A.; Awad, D.; Shaban, S.Y. Chitosan-based dithiophenolato nanoparticles: Preparation, mechanistic information of DNA binding, antibacterial and cytotoxic activities. *J. Mol. Liq.* **2020**, *318*, 114252. [CrossRef]
39. Elshami, F.I.; Ramadan, A.M.; Ibrahim, M.M.; Elmehasseb, I.M.; Al-Juaid, S.; Shaban, S.Y. Metformin Containing Nickel (II) Complexes: Synthesis, Structural Characterization, Binding and Kinetic Interactions with BSA, Antibacterial and in-vitro Cytotoxicity Studies. *Appl. Organometal. Chem.* **2019**, *34*, 5437. [CrossRef]
40. Shereef, H.A.; Shaban, S.Y.; Moemen, Y.S.; El-Khouly, M.E.; El-Nahas, A.M. Biophysicochemical studies of a ruthenium (II) nitrosyl thioether-thiolate complex binding to BSA: Mechanistic information, molecular docking, and relationship to antibacterial and cytotoxic activities. *Appl. Organomet. Chem.* **2022**, *35*, 6583. [CrossRef]
41. Lin, X.; Tang, D.; Yua, Z.; Feng, Q. Stimuli-responsive electrospun nanofibers from poly(N-isopropylacrylamide)-co- poly(acrylic acid) copolymer and polyurethane. *J. Mater. Chem. B* **2014**, *2*, 651. [CrossRef]
42. Badri, K.; Sien, W.; Shahrom, M.; Hao, L.; Baderuliksan, N.; Norzali, N. FTIR spectroscopy analysis of the prepolymerization of palm-based polyurethane. *Solid State Sci. Technol.* **2010**, *18*, 1–8.
43. Packham, D.E. Physiochemical aspects of polymer surfaces. In *International Journal of Adhesion and Adhesive*; Mittal, K.L., Ed.; Plenum Press: New York, NY, USA, 1983; pp. 583–594.
44. Choma, J.; Jamioła, D.; Augustynek, K.; Marszewski, M.; Jaroniec, M. Carbon–gold core–shell structures: Formation of shells consisting of gold nanoparticles. *Chem. Commun.* **2012**, *48*, 3972–3974. [CrossRef] [PubMed]
45. Huang, Y.-J.; Huang, C.-L.; Lai, R.-Y.; Zhuang, C.-H.; Chiu, W.-H.; Lee, K.-M. Microstructure and Biological Properties of Electrospun In Situ Polymerization of Polycaprolactone-Graft-Polyacrylic Acid Nanofibers and Its Composite Nanofiber Dressings. *Polymers* **2021**, *13*, 4246. [CrossRef] [PubMed]
46. Huang, Y.; Lu, J.; Xiao, C. Thermal and mechanical properties of cationic guar gum/poly(acrylic acid) hydrogel membranes. *Polym. Degrad. Stab.* **2007**, *92*, 1072. [CrossRef]
47. Drury, J.L.; Dennis, R.G.; Mooney, D.J. The tensile properties of alginate hydrogels. *Biomaterials* **2004**, *25*, 3187. [CrossRef] [PubMed]
48. Smart, S.K.; Cassady, A.I.; Lu, G.Q.; Martin, D.J. The biocompatibility of carbon nanotubes. *Carbon* **2006**, *44*, 1034–1047. [CrossRef]
49. Liu, Z.; Yang, Z.; Luo, Y. Swelling, pH Sensitivity, and Mechanical Properties of Poly(acrylamide-co-sodium methacrylate) Nanocomposite Hydrogels Impregnated with Carboxyl-Functionalized Carbon Nanotubes. *Polym. Compos.* **2012**, *33*, 665–674. [CrossRef]
50. Spinks, G.M.; Mottaghitalab, V.; Barhrami-Samani, M.; Whitten, P.G.; Wallace, G.G. Carbon-Nanotube-Reinforced Polyaniline Fibers for High-Strength Artificial Muscles. *Adv. Mater.* **2006**, *18*, 637. [CrossRef]
51. Xie, W.; Xu, P.; Wang, W.; Liu, Q. Preparation and antibacterial activity of a water-soluble chitosan derivative. *Carbohydr. Polym.* **2002**, *50*, 35–40. [CrossRef]
52. Denny, W.A.; Wakelin, L.P. Kinetic and equilibrium studies of the interaction of amsacrine and anilino ring-substituted analogues with DNA. *Cancer Res.* **1986**, *46*, 1717–1721.
53. Tomon, T.; Koizumi, T.; Tanaka, K. Electrochemical hydrogenation of [Ru(bpy)2(napy-kappaN)(CO)]2^{+}: Inhibition of reductive Ru-CO bond cleavage by a ruthenacycle. *Angew. Chem. Int. Ed.* **2005**, *44*, 2229–2232. [CrossRef]
54. Devi, V.S.; Chidi, O.O.; Coleman, D. Dominant effect of ethanol in thermal destabilization of bovine serum albumin in the presence of sucrose. *Spectroscopy* **2009**, *23*, 265–270. [CrossRef]
55. Chen, C.-K.; Lee, M.-C.; Lin, Z.-I.; Lee, C.-A.; Tung, Y.-C.; Lou, C.-W.; Law, W.-C.; Chen, N.-T.; Lin, K.-Y.A.; Lin, J.-H. Intensifying the Antimicrobial Activity of Poly [2-(tert-butylamino)ethyl Methacrylate]/Polylactide Composites by Tailoring Their Chemical and Physical Structures. *Mol. Pharm.* **2019**, *16*, 709–723. [CrossRef] [PubMed]
56. Beer, J.; Wagner, C.C.; Zeitlinger, M. Protein Binding of Antimicrobials: Methods for Quantification and for Investigation of its Impact on Bacterial Killing. *AAPS J.* **2009**, *11*, 1–12. [CrossRef] [PubMed]
57. Wright, J.D.; Boudinot, F.D.; Ujhelyi, M.R. Measurement and analysis of unbound drug concentrations. *Clin. Pharmacokinet.* **1996**, *30*, 445–462. [CrossRef] [PubMed]
58. Yano, Y.; Oguma, T.; Nagata, H.; Sasaki, S. Application of logistic growth model to pharmacodynamic analysis of in vitro bactericidal kinetics. *J. Pharm. Sci.* **1998**, *87*, 1177–1183. [CrossRef]

Disclaimer/Publisher's Note: The statements, opinions and data contained in all publications are solely those of the individual author(s) and contributor(s) and not of MDPI and/or the editor(s). MDPI and/or the editor(s) disclaim responsibility for any injury to people or property resulting from any ideas, methods, instructions or products referred to in the content.